Visual Target Tracking in Clay Pigeon Shooting Sports: Estimation of Flight Parameters and Throwing Range

Franz Andert[1], Simon Freudenthal[2] and Stefan Levedag[3]
[1]*Institute of Flight Systems, Unmanned Aircraft Dept., DLR (German Aerospace Center), Braunschweig, Germany*
[2]*Technische Universität Braunschweig, Braunschweig, Germany*
[3]*Head of the DLR-Institute of Flight Systems, Braunschweig, Germany*

Keywords: Image Processing, Stereo Triangulation, Sports Application, Rotating Disc, Flight Aerodynamics.

Abstract: This paper presents a method to estimate the trajectory and the flight distance of thrown pigeon clays. The basic principle is to measure the beginning of the flight with a camera system in order to forecast the further flight down to the ground impact. The demand of such advanced measuring methods arises from sporting clays competition regulations, where the launching machines have to be adjusted towards specific throwing angles and ranges. The presented method uses a wide-baseline stereo camera system (32 m camera distance) to measure the 3D clay disc positions, and the flight parameters are then identified by aerodynamic and kinematic considerations. This allows to estimate the whole path and the throwing distance, especially without a need to measure the ground impact itself. Applying this method to sporting clays facilities, the launching machines can be adjusted easier and more precisely, being advantageous especially for competitions. Additionally, it becomes possible to obtain the theoretical throwing distance on small sports areas bounded by nets or walls where a ground impact is not measurable.

1 INTRODUCTION

Clay pigeon shooting summarizes several precision sport disciplines where flying target discs have to be hit with firearms. There are variations within the disciplines, e.g. different sizes of the clay target, the position(s) from where to shoot, or the target flight speed, range, or launching elevation angle. A common ground is that the flying targets are launched with machines (traps). For competitions, the machines have to be adjusted precisely so that flight distance, direction and height specifications are achieved. The parameter values differ between the disciplines but a correct setting is usually a strict requirement.

This paper focuses on the setup of the *Skeet* discipline. As depicted in fig. 1, clay targets are launched from two houses, one from approx. 3 m above ground ("high house"), and the other from 1 m above ground ("low house"). The traps must be adjusted in a way so that the targets cross over a defined central point and that the flight distance is between 67 m and 69 m. Within manual adjustment, the conformance to these requirements is measured with a ring at the point where the targets have to fly through (fig. 2), and by measuring the distance between launcher and ground impact. Further information about the shooting range layout and the sporting rules can be found in (ISSF, 2013).

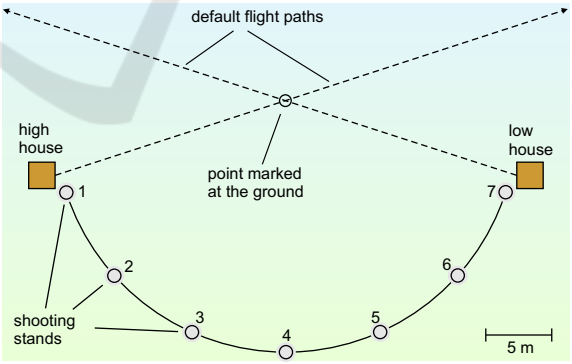

Figure 1: Schematic overview of Skeet shooting. The clay target is launched from the high and the low house and must be shot from the stands 1–7. Both flight paths must cross a point over the center marked at the ground.

2 PROBLEM STATEMENT

While the flight through the desired intersection point can be easily confirmed with a ring on top of a pole,

Andert, F., Freudenthal, S. and Levedag, S.
Visual Target Tracking in Clay Pigeon Shooting Sports: Estimation of Flight Parameters and Throwing Range.
DOI: 10.5220/0005674602950302
In *Proceedings of the 11th Joint Conference on Computer Vision, Imaging and Computer Graphics Theory and Applications (VISIGRAPP 2016) - Volume 3: VISAPP*, pages 297-304
ISBN: 978-989-758-175-5

the determination of the throwing range is impossible if the sports area is smaller than the typical flight distances (which is allowed by the rules) and surrounded by nets or walls. This is a common case for safety purposes, especially when multiple sports ranges are close to each other. Since competition rules require the throwing range value as a parameter to be determined, the adjustment process becomes circumstantial, e.g. by removing the safety nets during this process.

Figure 2: Skeet shooting range. High house with the launcher and the ring where the target disc has to fly through for launcher adjustment. The ring is removed afterwards.

To speed up this process, the idea is now to install a camera system to track the target discs. From the image-based measurements, the flight path is reconstructed and the flight parameters are estimated. This can be done by measurements while the target is flying inside the shooting range, which then allows to extrapolate the further path outside. With that, the throwing range is estimated independently of a flight interruption e.g. by safety nets. Figure 3 illustrates a setup with cameras which can be installed behind the shooting area and thus do not disturb the sports activities. To verify the flight path and throwing range estimation, the ground impact is measured as an additional reference (see also fig. 7 (b)), but there is no need to install this for further machine adjustment in a real application. For correct measurements, the cameras must be calibrated with intrinsic and extrinsic orientation parameters.

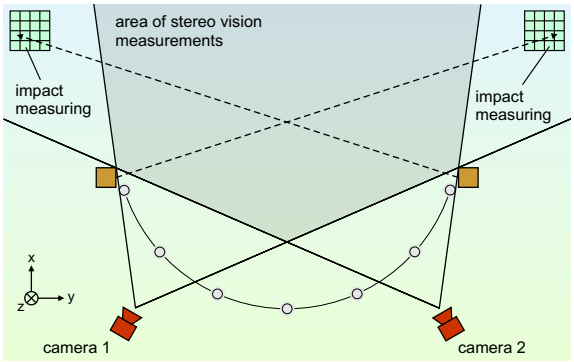

Figure 3: Camera setup at a Skeet shooting range. The beginning of the target's flight is measured by stereo imagery with a fixed camera system. Impact measurement is done only here to verify the presented approach.

3 THE FLIGHT OF ROTATING DISCS

3.1 Related Work

To estimate the disc's flight, this section introduces how the trajectory of the thrown target can be modeled in a suitable way. There is little scientific work dealing with thrown clay targets directly (such as (Denton, 2003) where a simulation setup is presented), however, the general physics of rotating discs can be applied here. A more focused view on the image-based detection of thrown objects is given e.g. in (Csordás et al., 2015). Note that the main topics of this paper are the flight kinematics, assuming general knowledge of image detection and tracking methods.

A comprehensive examination of the physics of rotating objects is presented in Lorenz's *Spinning flight* book (Lorenz, 2006). For example, the work gives a detailed mathematical description of the flight of a thrown frisbee. Its flight behavior is described as straightly ahead upwards in the beginning and with a veer to the left (meaning: against the direction of the ego-rotation) after the disc has reduced its velocity. Measurements with an instrumented frisbee-like disc can confirm these observations (Lorenz, 2005). From own observations, such a flight is apparently similar to a clay pigeon flight trajectory, just with slower speeds.

There is some other related work concerning disc flights, such as the report in (Hummel, 2003) which starts with a historical review of research investigations of different kinds of thrown things such as the flight of a javelin, frisbee or discus, and which gives a detailed mathematical description used here for the clay pigeon flight estimation. Another description is given by (Morrison, 2005) which includes the basic required equations. Possible applications are realistic simulations (e.g. (Denton, 2003), (Crowther and Potts, 2007)).

3.2 General Kinematics

Adapting the frisbee kinematics, a launched clay pigeon can be considered as a special case of a thrown rotating disc with its specific properties, see the constants in Tab. 1. These properties are known or can

be measured easily, including the moment of inertia tensor which is derived of the shape using Steiner's parallel axis theorem (see e.g. (Weisstein, 2007)). The determination of the trajectory (i.e. the flight state $\mathbf{x}$ over time, with 12 degrees of freedom describing 3D position, velocity, attitude, and rotation rates) refers to a differential equation system $\dot{\mathbf{x}} = f(\mathbf{x})$, dependent on initial conditions $\mathbf{x}_0$ and external influences, i.e. forces acting on the flying disc. In the presented context, the denoted flight state refers to an imaginary "hull" over the disc which does not rotate. Furthermore, the movement calculation requires additional assumptions and some initially unknown aerodynamic coefficients as discussed later.

Table 1: Flight state values, coefficients, and parameters.

Symbol(s)	Description
Flight State (components of $\mathbf{x}$), disc hull without spin	
$\mathbf{p}$	geodetic position: $(x,y,z)^\top$, local Cartesian
$\mathbf{v}$	velocity vector: $(u,v,w)^\top$, rotated to body
$\boldsymbol{\phi}$	geodetic attitude: $(\Phi,\Theta,\Psi)^\top$, Euler angles
$\boldsymbol{\omega}$	rotation rates: $(p,q,r)^\top$, body-fixed
Constants (default values or measured)	
A	disc area size: 0.0095 m^2
d	disc diameter: 0.11 m
m	disc mass: 0.105 kg
$\mathbf{I}$	inertia tensor: diag$(1.33,1.33,2.57)\cdot 10^{-4}$ kg m^2
g	gravity acceleration: 9.81 m/s^2 (default value)
ρ	air density: 1.184 kg/m^3 (default value)
Coefficients	
F_L, C_L	lift force, lift coefficient
F_D, C_D, K	drag force, drag coefficient, modeled helping constant
M, C_M	pitch moment, moment coefficient
N, C_N	yaw moment, moment coefficient
R, C_R	roll moment (neglected here)
Other variables	
$\mathbf{R}_{fg}$	rotation matrix: geodetic → flight body
$\mathbf{R}_{fa}$	rotation matrix: aerodynamic → flight body
$\mathbf{R}_{f\phi}$	rotation matrix: Euler angle change → flight body
v_a	aerodynamic speed
α	angle of attack
ω_{spin}	disc rotation (yaw rate inside hull)
t	time (numbered time stamps)

Fig. 4 illustrates the factors which have an influence on the disc's motion, being dependent on the velocity, the angle of attack (i.e. the angle between the direction of the velocity vector and the "forward" direction d_1 in the disc plane), and the rotation rates. Aerodynamic and gravity forces apply on different points, resulting in rotational moments. Following (Hummel, 2003), the occurrent forces can be transformed into forces and moments, both acting on the center of mass of the disc. While gravity can be assumed as static for a specific place, aerodynamic forces vary due to air conditions (wind, air pressure, etc.), the disc's shape and size, and the current flight speed and direction.

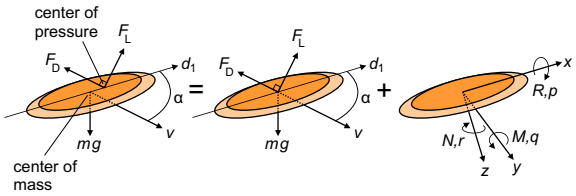

Figure 4: Forces and moments on a falling and rotating disc (cf. (Hummel, 2003)). The main influences are the gravity force (mg) and aerodynamic lift (F_L) and drag (F_D), dependent on velocity v and the angle of attack α. The forces applying on different points can be transformed into forces and moments (N,M,R), both acting on the center of mass.

3.3 Flight Trajectory Model

The equation system $\dot{\mathbf{x}} = f(\mathbf{x})$ to determine the flight trajectory can be derived from the forces as described in the given references. For the flight path calculations, the state $\mathbf{x}$ refers to an imaginary non-spinning hull around the disc. The body-fixed x-axis is along the direction of flight, i.e. it corresponds with the velocity vector. The state components are geodetic position $\mathbf{p}$ and attitude $\boldsymbol{\phi}$, and the hull-oriented velocity $\mathbf{v}$ and turn rates vectors $\boldsymbol{\omega}$. Following the flight kinematics in (Lorenz, 2005), the differential equations for the state components are denoted:

– Position (derived from velocity):

$$\dot{\mathbf{p}} = \mathbf{R}_{fg}^\top \cdot \mathbf{v} \tag{1}$$

– Velocity (from forces and rotation):

$$\dot{\mathbf{v}} = \frac{1}{m} \cdot \mathbf{R}_{fa} \begin{pmatrix} -F_D \\ 0 \\ -F_L \end{pmatrix} + \mathbf{R}_{fg} \begin{pmatrix} 0 \\ 0 \\ g \end{pmatrix} - \boldsymbol{\omega} \times \mathbf{v} \tag{2}$$

– Attitude (from turn rates):

$$\dot{\boldsymbol{\phi}} = \mathbf{R}_{f\phi} \cdot \boldsymbol{\omega} \tag{3}$$

– Turn rates (from pitch and yaw moments, and rotation):

$$\dot{\boldsymbol{\omega}} = \mathbf{I}^{-1} \left(\mathbf{R}_{fa} \left(\begin{pmatrix} 0 \\ M \\ 0 \end{pmatrix} + \boldsymbol{\omega} \times \left(\begin{pmatrix} 0 \\ 0 \\ N \end{pmatrix} \right) \right) + (\mathbf{I} \cdot \boldsymbol{\omega}) \times \boldsymbol{\omega} \right) \tag{4}$$

The eqs. 1–4 are general for dynamically balanced rigid bodies. Also general is the derivation of the transformation matrices, e.g. $\mathbf{R}_{fg}$ from the attitude $\boldsymbol{\phi}$ (see e.g. (Cai et al., 2011), pp. 23–34). There are acting forces and moments, and they are derived as follows: Within eq. 2, it is lift force (v_a: aerodynamic speed):

$$F_L = \frac{1}{2} C_L A \rho v_a^2 \tag{5}$$

with lift coefficient $C_L \approx C_{L_0} + C_{L_\alpha} \cdot \alpha$, which is approximately linear to the angle of attack in the considered limits ($-10° < \alpha < 30°$). Perpendicular to lift, the drag force F_D is

$$F_D = \frac{1}{2} C_D A \rho v_a^2 \tag{6}$$

with the drag coefficient $C_D \approx C_{D_0} + K \cdot C_L^2$. While the roll moment is minimal due to precession and thus neglected in eq. 4, the other moment components are modeled

$$M = \frac{1}{2} C_M A \rho v_a^2 d \tag{7}$$

with pitch moment coefficient $C_M \approx C_{M_0} + C_{M_\alpha} \cdot \alpha$, and

$$N = \frac{1}{2} C_N I_z \omega_{spin} A \rho v_a^2 d \tag{8}$$

with C_N as yaw moment coefficient. Here, ω_{spin} denotes the "real" rotation rate of the disc inside the non-rotating hull.

To derive a flight trajectory, an initial state $\mathbf{x}_0$ and the mentioned coefficients must be given. This is done with the help of camera measurements as described in the next section. As soon as the beginning of the flight is known by that, the model parameters and the full path can be derived by fitting the trajectory with the measurements. This is outlined in section 5.

Nevertheless, the model has some simplifications. With regard to the achievable accuracy, the influence of wind is of high importance, and the conversion between geodetic and aerodynamic coordinates (i.e. wind speed and direction) is assumed to be known and constant here. Wind can be measured with a weather station, however some very local wind gusts will have a negative influence on the forecast of the flight. Since there was no or almost no wind during the tests, this influence is neglected first of all. Another large effect is the influence of the disc rotation ω_{spin}. It is assumed to be known (here measured by taking video sequences of a marked disc from above), independent of the launcher settings, and rather undamped over the flight, which is a fair but not an exact approximation. There are remaining minor effects like roll moment, variations in air density and gravity, Earth curvature and rotation, and of course disc fabrication tolerances, but all of them are neglected due to their comparatively low influence or limited measurability.

4 3D MEASURING WITH A STEREO CAMERA

The camera-based measurement of the disc's flight follows the classical principles of multi-view imagery (e.g. (Hartley and Zisserman, 2000)). In the presented setup, the 3D positions are estimated from non-parallel stereo image sequences, and with a large baseline (>30 m) to achieve accurate results. Regarding the practical applicability, the 3D positions of the disc can be obtained from stereo or multi-view pairs if the following constraints are fulfilled:

1) The camera system is stationary and easy to calibrate. The calibration must determine intrinsic parameters (principal point, focal length, lens distortion) and extrinsic orientation (position and rotation related to an external coordinate system). One suitable method is Kwon's camera resectioning (Kwon, 1998). This method requires corresponding 2D image points and 3D objects, and it is basically a direct linear transform with non-linear optimization. For a field setup, 3D objects with distinctive markers can be installed and measured on the field once, which allows automatic re-calibration of the cameras if required.

2) Corresponding images from all the cameras must be recorded at equal times, requiring camera synchronization. Depending on the used camera system, this requires an external trigger input or visual hints to find images with (closely) equal exposure time stamps.

3) The thrown disc is visible in at least two images at a time so that the pixel position of the target (i.e. its center) can be triangulated, or, vice versa, a reprojection error minimization is unique. Segmentation and tracking require good image quality with respect to noise, lighting conditions, motion blur, and of course general visibility. Background subtraction helps a lot here. Fig. 5 shows an example of extracting a target position from an image.

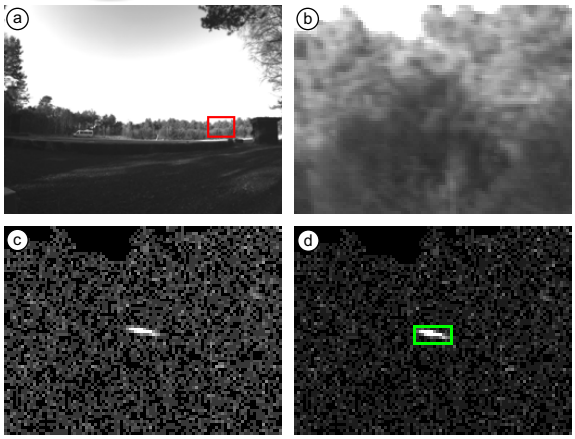

Figure 5: Example image of a flying clay disc. Full image (a), zoom to the image region of interest (b), background subtraction with amplified contrast (c), further filtering and clustering of the disc (d).

Successful disc segmentation might be followed by tracking, and corresponding region centroids can be assumed as homologous projections with chronological synchronism.

5 PATH FITTING AND PARAMETER OPTIMIZATION

Following sec. 3.3, a flight trajectory $\mathbf{x}_{1:t_{\max}} : \{\mathbf{x}_t\} | t \in \{1 \ldots, t_{max}\}$ can be derived from the initial state $\mathbf{x}_0$ and the required coefficients. Table 2 lists values, measured by instruments or hand estimate, yielding a trajectory that looks already like a thrown disc flight. Some of the values differ between the high and short house, and the investigation includes a short and a long launch as described in the test section. However, such kind of path calculation does usually not fit to camera observations. This means that the derived path is already erroneous in the beginning, resulting in a rather unqualified distance estimate.

Table 2: Initial flight state values and coefficients.

Variables	**Initial values**
ω_{spin}	73 1/s (rad/s)
α	0.001 (rad)
$\mathbf{p}$	(-5.1, -19.4, -3.15)$^\top$ m (high house);
	(-5.3, 19.2, -1.42)$^\top$ m (low house)
$\mathbf{v}$	$(\cos(\alpha), 0, \sin(\alpha))^\top \cdot 30$ m/s
$\boldsymbol{\phi}$	$(0, \Theta, \Psi)^\top$ (rad), with
	Θ: 0.187 (long), 0.138 (short launch) at high house
	Θ: 0.285 (long), 0.187 (short launch) at low house
	Ψ: 1.31 (high house), 4.44 (low house)
$\boldsymbol{\omega}$	$(0, 0, 0)^\top$
Coefficients	**Initial value for optimization**
C_{L_0}	0.1
C_{L_α}	1.9
C_{D_0}	0.2
K	0.8
C_{M_0}	-0.05
C_{M_α}	0.6
C_N	100

As depicted in Fig. 6, the idea is now to optimize the roughly guessed or unknown parameters by finding an optimized parameter set so that the resulting trajectory will fit to the observations. With regard to the aspired application, camera measurements will be available only in the first phase of the flight, and they are used to forecast the rest of the flight towards the ground impact. To validate this procedure later in the test section, hand-measurements of the impact are taken as a reference for the distance estimate.

The optimization procedure works as follows: Let $\mathbf{c}$ be the coefficient vector

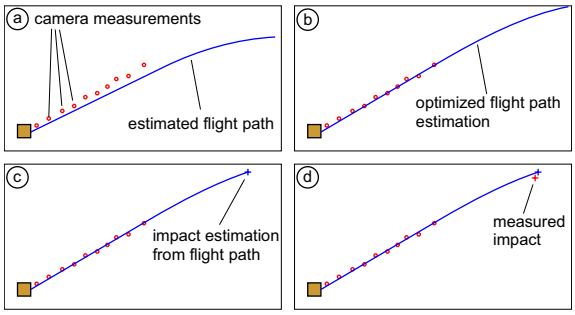

Figure 6: Principle to estimate the flight trajectory and throwing range: camera measurements from a launched disc and trajectory estimation from rough (i.e. assumed or guessed) external parameters (a), parameter optimization by fitting trajectory estimate and measurements (b), derivation of the ground impact of the disc, i.e. intersection of flight path and ground plane (c), comparison of estimated impact and hand-measured impact to verify the path estimation (d).

$(C_{L_0}, C_{L_\alpha}, C_{D_0}, K, C_{M_0}, C_{M_\alpha}, C_N)^\top$ to be optimized and, accordingly, $\mathbf{x}(\mathbf{c})_{1:t_{\max}}$ the mapping function $\mathbf{c} \rightarrow \mathbf{x}_{1:t_{\max}}$ dependent on $\mathbf{c}$ (and of course the fixed inputs $\mathbf{x}_0, \omega_{spin}, \alpha_0$). Then, $\mathbf{p}(\mathbf{c})_{1:t_{\max}}$ denotes the disc position over time as a subset of $\mathbf{x}(\mathbf{c})_{1:t_{\max}}$. Further, let $\mathbf{Q}_i(\mathbf{p}_t)$ be the projection of a single disc position $\mathbf{p}$ at time t to the image plane of the i-th camera. With the image measurements $\mathbf{q}_{i,t}$ with timestamps $t \in T \subseteq \{1, \ldots, t_{\max}\}$, and by using n cameras, a parameter set $\mathbf{c}$ which produces a trajectory that fits to the image measurements, solves

$$\arg\min_{\mathbf{c}} \sum_{t \in T} \sum_{i=1}^{n} \| \mathbf{Q}_i(\mathbf{p}_t(\mathbf{c})) - \mathbf{q}_{i,t} \|. \qquad (9)$$

This least reprojection error solution for $\mathbf{c}$ can be derived with non-linear optimization, implemented here with a Levenberg-Marquardt algorithm. It requires an approximate initialization (see again Tab. 2) and at least two cameras with significant observation differences, i.e. a large stereo baseline. Within the sequence of succeeding images, few missing observations (e.g. from bad image quality) are not critical.

6 TEST AND EVALUATION

The evaluation of the presented method requires to measure the 3D path of the flying disc, to make an estimate of its path by these measurements in order to predict the impact and throwing distance, and to compare this prediction with a measurement of the true impact. Accurate measurements and predictions are achieved with the following setup:

1) The cameras (Fig. 7(a)) are placed with a good view on the expected disc flight, here at 4 m above

ground and with a stereo baseline of approximately 33 m. The usable horizontal field of view is around 70° for each camera, the evaluation of pixels at the highly distorted image edges is avoided.

2) Visual landmarks for camera calibration are placed on the sports area within the camera fields of view. Their 3D position is measured with a total station with a 3D accuracy of around 1 cm (laser measurement, see Fig. 7(c)). Camera calibration is performed with images of the placed landmarks, and the camera positions can be roughly validated with total station measurements.

3) To verify the suitability of the path and distance calculation, the estimated impact position is compared to the true impact which must be measured by hand. A canvas with coordinate grid for ground impact measuring is placed at the desired impact positions (Fig. 7(b)). The canvas grid coordinates are also measured with the total station. Remember that such a ground impact measurement is not available in the application case.

4) After the preparations, measurements of thrown discs are taken. Each launched disc flight is recorded with two cameras (here: GoPro Hero 3 Black, WiFi remote control). In the presented case, the cameras use an internal WiFi-based exposure control. To validate the simultaneousness of both camera sequences, a light with short blinking (Fig. 7(d)) is placed in the shared field of view. The light impulses (approx. 20–30 ms duration) are later visible in both image sequences. The cameras record images with 1280 x 720 pixels and with 120 frames per second. Following (Matthies and Shafer, 1987) and assuming one pixel accuracy of the target within the images, the 3D uncertainty from triangulation is roughly 4 cm at all axes just after the launch, and around 8 cm later at higher distances to the cameras.

5) As a reference, the ground impact position on the canvas is measured by hand and marked on the canvas.

6) For each recorded launch, the 3D path of the thrown disc is calculated. Based on that, the flight parameters are estimated, and the further flight path outside the visible area down to the impact is extrapolated. This returns an impact position (and with that, the throwing range) estimation which is compared to the manual measurement on the canvas.

7) Weather conditions are measured. Important facts: Clear sky, mostly no wind.

The test campaign includes sixteen launches from both houses. It contains two different configurations of long and short throwing ranges depending on the adjustment of the launching machine. Table 3 presents some facts about all flights: especially the measured throwing range and the error of the estimation towards this range measurement. For each of the four used launching configurations (low or high house, and machine adjustment for a long or a short throw), one example plot of the measured and estimated flight path is shown in the figures 8 to 11. All plots include the estimated path (–) and impact (•), stereo measurements (·) and the hand-measured reference impact (+) of the particular clay target. The plots show also the impacts of the other clay targets, marked with a light gray (+) sign.

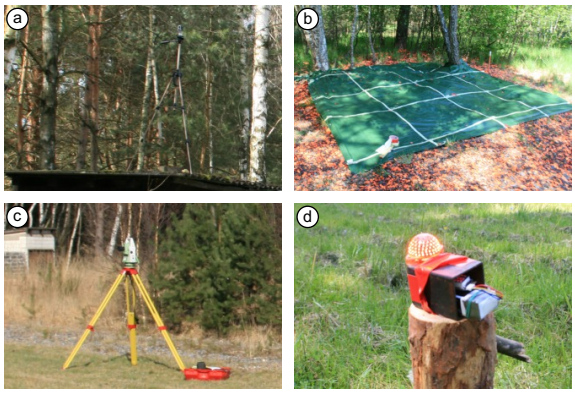

Figure 7: Measuring equipment: camera with 4 m height above ground (a), measuring the ground impact on a canvas with known coordinates (b), total station for camera landmark and other coordinate measurements (c), blinking light to confirm the stereo camera synchronization (d).

Table 3: Throwing distances and absolute values of the estimation errors.

No.	house	launch	throw dist.	estim. err.	plot
1	low	long	68.38 m	2.61 m	Fig. 8
2	low	long	68.22 m	3.22 m	
3	low	long	69.54 m	2.88 m	
4	low	long	68.27 m	3.23 m	
5	low	long	69.09 m	3.25 m	
6	low	short	55.03 m	1.31 m	
7	low	short	52.71 m	1.21 m	
8	low	short	56.45 m	2.97 m	
9	low	short	56.47 m	2.79 m	
10	low	short	54.76 m	1.07 m	Fig. 9
11	high	long	61.08 m	1.14 m	Fig. 10
12	high	long	62.39 m	0.54 m	
13	high	long	63.18 m	1.17 m	
14	high	short	49.07 m	4.07 m	
15	high	short	52.08 m	1.05 m	Fig. 11
16	high	short	53.54 m	0.74 m	

Derived from the facts in Table 3, the most obvious results are a throwing range variation of about ±2 m for a specific launcher configuration. Possible reasons for this uncertainty may be the available im-

precision of the launching machines itself, irregularities of the disc (tolerances, scratches etc.), but mainly external influences like wind gusts. Another result is the observed uncertainty of the estimation of up to 4 m, possibly due to bad measurements (e.g. errors within camera calibration or systematic pixel uncertainty) or due to imprecise or wrongly assumed input parameters for the flight path estimation (especially wind parameters and disc spin).

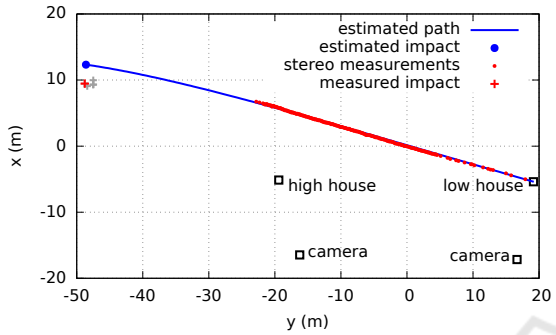

Figure 8: Measured and estimated clay target flight, launched from the low house with long throwing distance.

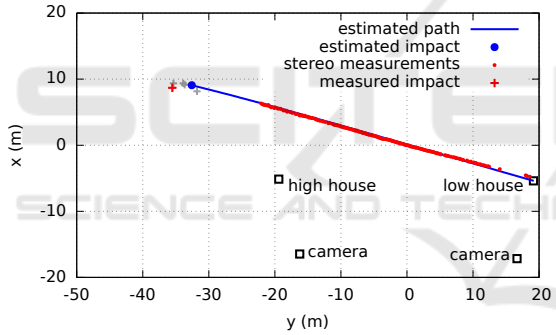

Figure 9: Measured and estimated clay target flight, launched from the low house with short throwing distance.

7 CONCLUSION AND FUTURE APPLICABILITY

The paper presents a method to estimate the path of flying pigeon clay targets, i.e. thrown rotating discs. The method consists of a model derived by the acting forces, and by camera measurements to obtain uncertain parameters of this model. Based on the visual observed, a fitting trajectory can be determined and further extrapolated down to the impact position. It is shown that the impact position can be estimated with an accuracy of about three meters only with visual measurements of the beginning of the flight, i.e. the first half just after launch where the thrown disc is still inside the sporting area. Based on that, it becomes

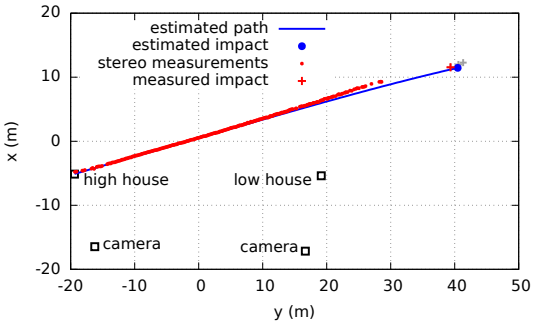

Figure 10: Measured and estimated clay target flight, launched from the high house with long throwing distance.

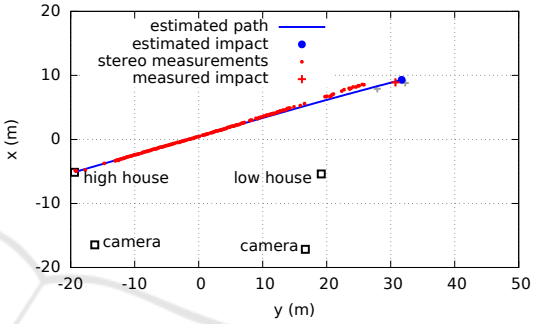

Figure 11: Measured and estimated clay target flight, launched from the high house with short throwing distance.

possible to estimate the throwing range without measuring the impact itself. The desired application is the target launching machine adjustment in order to fulfill the requirements of the specified sporting clays discipline. With the presented method, launching machine adjustment will be faster and easier. Additionally, the method is very convenient for sports areas where no target impact is measurable due to surrounding safety nets.

There is some potential for further optimization and accuracy enhancement, especially with regard to wind considerations and towards modeling the disc spin damping. However, the principle is close to practical applications. For a sports setup, this means to install fixed camera systems at the sporting area together with some non-disturbing or removable visual landmarks with known coordinates for the camera calibration routine. Further, measurement and path estimation are to be automated and integrated into an easily usable software. After this is achieved, games are going to avail themselves of the new method.

ACKNOWLEDGEMENTS

Special thanks go to Stephan Lange from WTC Wolfsburg for the provision of the sports facilities.

REFERENCES

Cai, G., Chen, B., and Lee, T. (2011). *Unmanned Rotorcraft Systems: Advances in Industrial Control*. Springer.

Crowther, W. J. and Potts, J. R. (2007). Simulation of a spin-stabilised sports disc. *Sports Engineering*, 10(1):3–21.

Csordás, R., Havasi, L., and Szirányi, T. (2015). Detecting objects thrown over fence in outdoor scenes. In *Proceedings of the 10th International Conference on Computer Vision Theory and Applications*, pages 593–599.

Denton, A. (2003). A 3d modelling and visualisation system for clay pigeon shooting. Master's thesis, Imperial College, London.

Hartley, R. and Zisserman, A. (2000). *Multiple View Geometry in Computer Vision*. University Press, Cambridge.

Hummel, S. A. (2003). Frisbee flight simulation and throw biomechanics. Master's thesis, Office of Graduate Studies of the University of California, Davis.

ISSF (2013). International shooting sport federation: Official statutes and regulations. url: http://www.issf-sports.org/documents/rules/2013/ISSFRuleBook2013-2ndPrint-ENG.pdf, Version 01/2014. Skeet setup at pp. 230–233.

Kwon, Y.-H. (1998). Direct linear transform method. url: http://www.kwon3d.com/theory/dlt/dlt.html.

Lorenz, R. D. (2005). Flight and attitude dynamics of an instrumented frisbee. *Measurement Science and Technology*, 16:738–748.

Lorenz, R. D. (2006). *Spinning Flight: Dynamics of Frisbees, Boomerangs, Samaras, and Skipping Stones*. Springer.

Matthies, L. and Shafer, S. A. (1987). Error modeling in stereo navigation. *IEEE Journal of Robotics and Automation*, 3(3):239–248.

Morrison, V. R. (2005). The physics of frisbees. *Electronic Journal of Classical Mechanics and Relativity*.

Weisstein, E. W. (2007). Parallel axis theorem. url: http://scienceworld.wolfram.com/physics/ParallelAxisTheorem.html.